RESEARCH ARTICLE

High-resolution projections of extreme heat in New York City

Luis E. Ortiz[1] [ORCID] | Jorge E. González[1] | Radley Horton[2] | Wuyin Lin[3] | Wei Wu[4] | Prathap Ramamurthy[1] | Mark Arend[1] | Robert D. Bornstein[5]

[1]Department of Mechanical Engineering, The City College of New York, New York, New York

[2]Lamont-Doherty Earth Observatory, Columbia University Earth Institute, New York, New York

[3]Department of Environmental & Climate Sciences, Brookhaven National Laboratory, Upton, New York

[4]Coast Survey Development Laboratory, Office of Coast Survey, National Ocean Service, NOAA, Silver Spring, Maryland

[5]Department of Meteorology, San Jose State University, San Jose, California

Correspondence
Luis E. Ortiz, Department of Mechanical Engineering, The City College of New York, New York, NY 10031.
Email: lortiz10@citymail.cuny.edu

Abstract

Heat waves impact a wide array of human activities, including health, cooling energy demand, and infrastructure. Cities amplify many of these impacts by concentrating large populations and critical infrastructure in relatively small areas. In addition, heat waves are expected to become longer, more intense, and more frequent in North America. Here, we evaluate combined climate and urban surface impacts on localized heat wave metrics throughout the 21st century across two emissions scenarios (RCP4.5 and RCP8.5) for New York City (NYC), which houses the largest urban population in the United States. We account for local biases due to urban surfaces via bias correcting with observed records and urbanized 1-km resolution dynamical downscaling simulations across selected time periods (2045–2049 and 2095–2099). Analysis of statistically downscaled global model output shows underestimation of uncorrected summer daily maximum temperatures, leading to lower heat wave intensity and duration projections. High-resolution dynamical downscaling simulations reveal strong dependency of changes in event duration and intensity on geographical location and urban density. Event intensity changes are expected to be highest closer to the coast, where afternoon sea-breezes have traditionally mitigated summer high temperatures. Meanwhile, event duration anomaly is largest over Manhattan, where the urban canopy is denser and taller.

KEYWORDS
climate impacts, climate projections, dynamical downscaling, heat waves, urban

1 | INTRODUCTION

Heat waves caused the second most weather-related fatalities in the United States in the last decade (National Weather Service, 2015), with 97 directly attributed deaths per year between 2008 and 2017 and 107 in 2017 alone. New York City (NYC) is the most heavily populated city in the United States, with over 8 million residents, more than double of the second highest population, Los Angeles. Studies have shown that longer, more intense heat waves in the United States are associated with increases in mortality (Anderson

and Bell, 2010), metrics that are projected to increase throughout the 21st century (Meehl and Tebaldi, 2004). Furthermore, these summertime increases in heat-related mortality may not be offset by decreases in cold-weather deaths in Manhattan, New York (Li et al., 2013), the city's most densely populated borough. Warm weather also increases energy demand for air conditioning (Le Comte and Warren, 1981; Santamouris et al., 2001; Miller et al., 2008; Ortiz et al., 2018a), although decreases in winter heating may partially or completely offset the cost of increased cooling (Rosenthal et al., 1995). Infrastructure and health impacts

may also occur simultaneously, as was shown for the 2003 NYC city-wide blackout, which saw a 25% increase in non-accidental deaths (Anderson and Bell, 2012).

In addition, cities interact with the atmospheric boundary layer by introducing heat source and storage terms into the surface energy balance (Oke, 1988) and limiting natural cooling processes (e.g., soil moisture evaporation). These processes, in general, lead to higher temperatures in cities compared to surrounding suburban and rural areas, a phenomenon called the urban heat island (UHI). These added surface energy terms modify the atmospheric boundary layer, potentially increasing convective motions, elevating the daytime convective layer and weakening night-time stable layers. In NYC, the complex nature of its urban landscape and its geographical location has historically led to a spatially and temporally heterogeneous UHI (Gaffin et al., 2008).

Urban surface–atmosphere feedbacks can exacerbate heat wave conditions in cities. For example, Li and Bou-Zeid (2013) found UHI intensification in the Baltimore, MD, while Ramamurthy et al. (2017) found the NYC UHI reached up to 10°C during the June 2016 heat wave, both attributing synergistic interactions between heat waves and urban surfaces to decreased evaporative cooling over cities. In the July 3–8, 2010 heat wave in NYC, urban contributions to afternoon near-surface temperatures were 2°C larger than on preceding days (Ortiz et al., 2018b), due to a combination of decreased evaporative cooling, modified wind speeds, and increased anthropogenic heat. Li et al. (2016) found enhancement of the Beijing Metropolitan Area UHI due to wind profile changes during heat waves, similar to results from Founda and Santamouris (2017), who found UHI intensification in Athens, Greece to be highly dependent on wind magnitude and direction. Others have found evidence of UHI intensification during heat waves in Madison, WI (1.8°C daytime, 5.3°C night-time; Schatz and Kucharik, 2015). However, Scott et al. (2018) showed in a multi-city, multi-year study that in 70% of the cities analysed, rural temperatures increased faster than urban temperatures, leading to lower UHI magnitudes during warm days. This underscores the need for studies of the underlying land surface processes that determine urban temperatures during hot days and how they vary across different regions and urban forms.

Meanwhile, study of climate impacts and development of future projections has traditionally relied on general circulation models (GCMs), which operate at spatial resolutions of ~100 km. While useful to evaluate global- and even continental-scale climate impacts, their coarse grid spacing limits their potential to represent locally significant processes due to complex orography, coastlines, and heterogeneous land cover (e.g., cities), as well as fine-scale atmospheric processes (e.g., clouds, convection). Attempts to overcome these limitations often involve downscaling techniques to add information at finer scales than GCM native grids. There are two approaches to achieve this: statistical and dynamical. The former often involves using extraneous climatological records to transform coarse GCM output to more closely match records at specific locations, often by transforming their distribution. Dynamical downscaling uses GCM output as initial and boundary conditions to a limited area numerical weather prediction system, which then solves the systems of equations describing the behaviour of the land surface and atmosphere. Here, we present projections based on both a statistically downscaled GCM ensemble and high-resolution (1-km horizontal grid spacing) dynamical downscaling to explore temporal and geospatial variability of heat wave metrics throughout the 21st century. Our approach aims to incorporate urban surface processes that may not be adequately represented in GCMs due to limitations in model resolution and parameterizations.

2 | METHODS

2.1 | Heat wave definitions

There is no definite definition of a heat wave, with various definitions found in the literature addressing the needs of particular communities. Smith et al. (2013) showed that in the US Northeast, heat wave days have increased across 15 definitions. Here, we define a heat wave following regional U.S. National Weather Service in New York, which labels a heat wave as at least three consecutive days with temperatures of at least 90°F (32.22°C; National Weather Service, 2018). Results will use two metrics to describe heat wave projections:

- Mean heat wave intensity: Mean daily maximum temperature (°C) of all events in a given year.
- Mean heat wave duration: Mean heat wave duration, in days, of all events in a given year.

2.2 | Observations and GCM ensemble

Observation records within NYC were taken from the Global Historical Climatological Network (GHCN)-Daily (Menne et al., 2012) weather stations, specifically at Central Park, John F. Kennedy Airport (JFK), and LaGuardia Airport (LGA). These stations were selected for having long, mostly uninterrupted measurement periods spanning multiple decades. GHCN-Daily records are quality-checked, but not homogenized. Although all three stations are located within NYC city limits, differences in their surrounding land cover characteristics and distance to the coast impact each

record's temperatures. For example, Central Park station, although located within the densely packed borough of Manhattan, is surrounded by grass and trees, whereas LGA and JFK are located close to the north and south shores of Queens borough (Figure 1, inset), respectively.

Ensemble members used in the single point statistically downscaled projections belong to the Fifth Climate Model Inter-comparison Project (CMIP5; Taylor *et al.*, 2012) and are detailed in Table 1. For each model, we consider daily maximum temperature from the summers (June–July–August) between 2006 and 2100. Two scenarios are considered based on the representative concentration pathways (van Vuuren *et al.*, 2011), RCP4.5 and RCP8.5, which use a combination of policy, technology, and demographic projections to estimate global radiative forcing paths. RCP4.5 (Thomson *et al.*, 2011) is considered a medium emissions scenario, with increasing global radiative forcing that stabilizes by 2100 at 4.5 W/m^2. RCP8.5 (Riahi *et al.*, 2011) is a high emission or "business as usual" scenario, with increasing radiative forcing reaching around 8.5 W/m^2 by end of century.

2.3 | Statistical bias correction

Mean event duration (days/event) and intensity (event maximum temperature) were computed using a composite
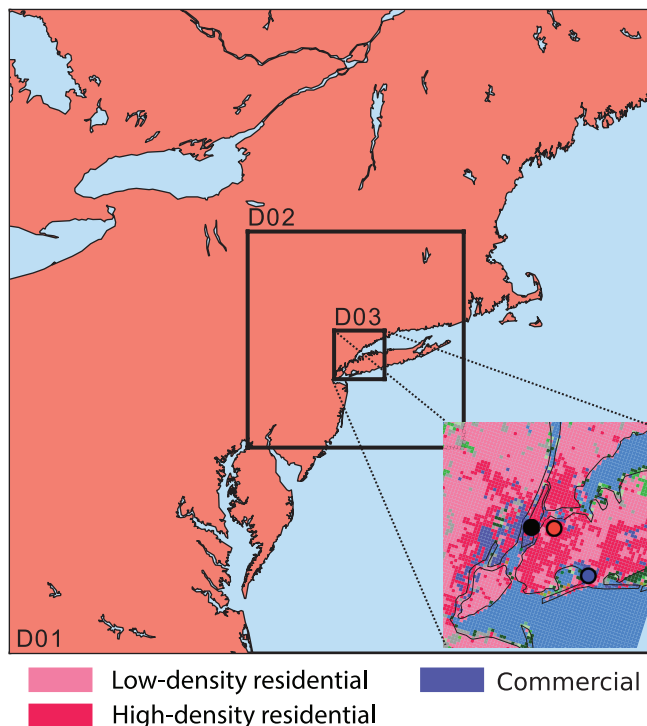
temperature record based on the daily maximum temperature averaged across all three urban stations. These stations were selected due to (a) their proximity to NYC and (b) their long, consistent records. These historical records were in turn used to perform bias correction GCM projections following the work of Piani *et al.*, 2010 and Hawkins *et al.*, 2013. The bias correction technique corrects for model mean and standard deviation using a linear model,

$$T_{BC} = \bar{T}_{Obs, REF} + \frac{\sigma_{Obs, REF}}{\sigma_{GCM, REF}} \left(\bar{T}_{GCM, RAW}(t) - \bar{T}_{GCM, REF} \right).$$

Here, T refers to the temperature records and σ refers to its standard deviation. Subscripts Obs and GCM refer to observation and model data, respectively, while REF and RAW refer to the reference (2006–2015) and entire projection periods (2006–2099). The over bar ($\bar{}$) marker denotes use of the average for the specified data set and time period. All three stations used were missing a minimal amount of data (<2%) which were removed from the record before computing the mean and standard deviation. Uncertainties in the projections were quantified by use of a 26-model ensemble. GCM horizontal resolution is often >100 km, so in many cases there was no grid point that coincides with NYC city limits. For all models, the geographically closest land grid point to NYC was used to develop all projections. A single point is used due to GCMs' generally coarse resolution, meaning that other grid points might be too distant to NYC to provide relevant information.

2.4 | Urbanized dynamical downscaling

This work uses the Weather Research and Forecasting (WRF) model (Skamarock *et al.*, 2008) to study interactions between cities and the atmosphere during extreme heat events. Model initial and boundary conditions are derived from the National Center for Atmospheric Research (NCAR) bias-corrected Community Earth System Model (CESM) data set (Monaghan *et al.*, 2014). This data have been bias-corrected using ERA-Interim reanalysis across all vertical levels (Bruyère *et al.*, 2014). This bias correction method decomposes all GCM variables into a seasonal and trend component and then substitutes the seasonal component of the GCM with that of the reanalysis. This approach was found to improve representation of precipitation, as well as correcting cooler 2-m temperature biases by 2–3°C.

Simulations use one parent domain at 9-km grid spacing with two subsequent nested domains, each reducing grid spacing by a factor of 3, reaching 1-km resolution (Figure 1). In order to account for processes critical to urban climate, an urban parameterization is required. In particular, we use the building effect parameterization (BEP) developed

FIGURE 1   Dynamical downscaling parent (D01) and nested domains (D02, D03) used in all simulations. Inset shows urban PLUTO-derived land use classification for D03. Black, red, and blue circles indicate the location of the Central Park, LGA, and JFK weather stations [Colour figure can be viewed at wileyonlinelibrary.com]

TABLE 1 Twenty-six-model ensemble and centre-of-origin used in single point heat wave projections

Centre	Model	Resolution (lat. × lon.)	Selected coordinate (lat., lon.)
Commonwealth Scientific and Industrial Research Organization: Bureau of Meteorology (Australia)	ACCESS1.0 ACCESS1.3	1.25 × 1.875° 1.25 × 1.875°	41.25°, −73.125° 41.25°, −73.125°
Canadian Centre for Climate Modeling and Analysis (Canada)	CanESM2	2.7906°× 2.8125°	40.46°, −73.125°
National Center for Atmospheric Research (United States)	CCSM4	0.9424 × 1.25°	40.99°, −73.75°
Centro Euro-Mediterraneo per i Cambiamenti Climatici (Italy)	CMCC-CM CMCC-CMS	0.7484 × 0.75° 3.7111 × 3.75°	40.79°, −74.25° 40.10°, −73.125°
Centre National de Recherches Météorologiques/Centre Européen de Recherche et de Formation Avencée en Calcul Scientifique (France)	CNRM-CM5	1.4008 × 1.40625°	41.32°, −74.53°
Commonwealth Scientific and Industrial Research Organization/Queensland Climate Change Centre of Excellence (Australia)	CSIRO-Mk3.6.0	1.8653 × 1.875°	40.103°, −73.125°
NOAA Geophysical Fluid Dynamics Laboratory (United States)	GFDL-ESM2G GFDL-ESM2M	2.0225 × 2° 2.0225 × 2°	41.46°, −73.75° 41.46°, −73.75°
NASA Goddard Institute for Space Studies (United States)	GISS-CM3 GISS-E2-H GISS-E2-R	2 × 2.5° 2 × 2.5° 2 × 2.5°	41.0°, −73.75° 41.0°, −73.75° 41.0°, −73.75°
Met Office Hadley Centre (UK)	HadGEM2-AO HadGEM2-CC HadGEM2-ES	1.25 × 1.875° 1.25 × 1.875° 1.25 × 1.875°	41.25°, −73.125° 41.25°, −73.125° 41.25°, −73.125°
Institut Pierre Simon Laplace (France)	IPSL-CM5A-LR IPSL-CM5A-MR IPSL-CM5B-LR	1.8947 × 3.75° 1.2676 × 2.5° 1.8946 × 3.75°	40.74°, −75.0° 40.56°, −75.0° 40.74°, −75.0°
Japan Agency for Marine-Earth Science and Technology, Atmosphere and Ocean Research Institute/National Institute for Environmental Studies/Japan Agency for Marine-Earth Science and Technology (Japan)	MIROC-ESM MIROC-ESM-CHEM MIROC5	2.7906 × 2.8125° 2.7906 × 2.8125° 1.4008 × 1.40625°	40.46°, −73.125° 40.46°, −73.125° 41.32°, −74.53°
Max Planck Institute for Technology (Germany)	MPI-ESM-LR MPI-ESM-MR	1.8653 × 1.875° 1.8653 × 1.875°	40.103°, −73.125° 40.103°, −73.125°
Meteorological Research Institute (Japan)	MRI-CGCM3	1.12148 × 1.125°	40.93°, −74.25°
Institute for Numerical Mathematics (Russia)	INM-CM4	1.5 × 2°	41.25°, −74.0°

by Martilli *et al.* (2002). BEP is a multi-layer urban canopy parameterization, possessing an internal coordinate system that resolves dynamical and energy fluxes between the urban canopy and the atmosphere. Urban momentum and energy fluxes are then added to adjacent WRF grid points, modifying thermodynamic and dynamical characteristics of the atmosphere. BEP represents mechanical impacts of the urban canopy as sinks in the momentum equation, as well as radiation blocking and reflection between walls and roofs. In addition to these building surface effects, we include the building energy model (BEM) from Salamanca *et al.* (2010). This parameterization adds building envelope anthropogenic heat fluxes to BEP by modelling air conditioning demand. Air conditioning target temperature was set to 24.85°C, with a target specific humidity of 0.1 g_{vapor}/kg_{air}.

BEP and BEM have also been modified to account for latent heat fluxes from air conditioning, based on the work of Gutierrez *et al.* (2015a) as well as effects of varying building packing density on drag coefficient (Gutiérrez *et al.*, 2015b). Cooling towers use evaporative cooling processes to remove heat from water used in air conditioning systems. This evaporative cooling effectively partitions urban heat fluxes into sensible and latent, adding a hydrological component to BEM. Gutiérrez *et al.*, 2015b
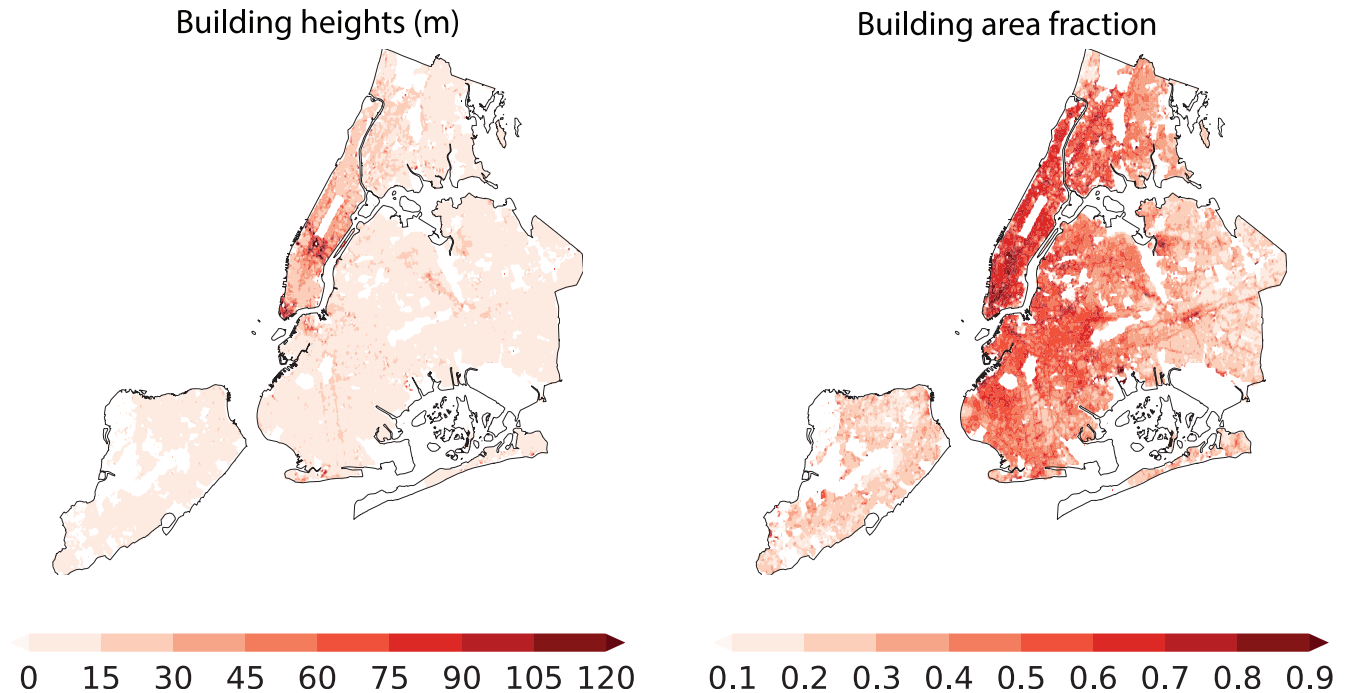
FIGURE 2 Building plant area fraction (left) and building height (right) parameters used in all simulations. Data are aggregated at 1-km grid spacing before ingesting into the urban WRF model [Colour figure can be viewed at wileyonlinelibrary.com]

implemented impacts of building packing density into the BEP code following results from Reynolds averaged numerical simulations (RANS) of Santiago *et al.* (2008), who related buildings' drag coefficient to their packing density through a series of experiments, as follows:

$$C_{eq}(\lambda_p) = \begin{cases} 3.32\lambda_p^{0.47} \text{ for } \lambda_p \leq 0.29 \\ 1.85 \text{ for } \lambda_p > 0.29 \end{cases}.$$

Here, C_{eq} is the urban canopy sectional drag coefficient as a function of λ_p, the building area fraction. This equation was fitted from the RANS results as a compromise between accuracy and simplicity; the choice of an empirical equation cannot be physically interpreted. In order to maximize the utility of the variable drag formulation, urban canopy parameters, including building area fraction and building height, were ingested into all simulation runs based on the Property Land-Use Tax-lot Output (PLUTO; Figure 2). PLUTO is a public data set that includes building physical trait data including footprint area, number of floors, and use type. Building heights were computed by assuming a floor height of 5 m, while building area was approximated by subtracting non-floor area (e.g., parking) from lot total area. Urban canopy parameters were interpolated into the model high-resolution domain with a horizontal grid spacing of 1 km. Gutiérrez *et al.* (2015b) showed that these modifications and inclusion of high-resolution urban canopy parameters improved model winds and temperature vertical profiles

when tested over an NYC domain. Tables 2 and 3 summarize the physics parameterizations used in all simulations.

3 | RESULTS

3.1 | Observed changes

As detailed in section 2, NYC houses three weather stations with at least 50 years of operation. The Central Park weather station has been in operation since 1869, while the LGA and JFK records go back as far as 1939 and 1959, respectively. Summer annual mean daily maximum temperatures, summarized in Figure 3, show increasing linear trends at a rate of 0.11°C/decade for Central Park and 0.13°C/decade for LGA, significant at $p < .01$, while JFK increases at 0.13°C/decade (not significant at $p < .01$). JFK median temperatures are

TABLE 2 Model configuration used for all WRF simulations

Parameter	Value
Spin-up (days)	4
Time step (seconds, D01, D02, D03)	45, 15, 5
Domain size (grid points)	85 (north–south), 82 (east–west)
SST update	Daily
Simulation period	Jun 1 to Aug 31 (plus spin-up)

Note: Values are presented for domain D03, unless otherwise specified.

TABLE 3 Model physics parameterizations used throughout all numerical experiments

Parameterization	Option	Active domain
Cumulus	Kain-Fritsch (Kain, 2004)	D01, D02
Microphysics	WSM6 (Hong and Lim, 2006, p. 6)	D01, D02, D03
Boundary Layer	Mellow-Yamada-Janjic (Nakanishi and Niino, 2006)	D01, D02, D03
Land Surface	Noah Land Surface Model (Tewari *et al.*, 2004)	D01, D02, D03
Urban Physics	BEP (Martilli *et al.*, 2002) BEM (Salamanca *et al.*, 2010) Cooling Tower (Gutiérrez *et al.*, 2015a) Urban Drag Coefficient (Gutiérrez *et al.*, 2015b)	D03

cooler than Central Park and LGA by ~1°C due to south/-southwesterly sea-breeze typical to the area (Gedzelman *et al.*, 2003). Sea-breeze patterns have been shown to be an important factor in the formation and daily cycle of the NYC UHI. Studies have found that on days when a sea-breeze develops, UHI formation is delayed, with its centre pushed towards the northwest of the city and neighbouring New Jersey. At night, a land breeze forms, moving the UHI centre closer to the southeast coastline.

Heat waves in NYC are defined as at least 3 days with temperatures reaching at least 90°F (32.22°C). Station records show that the likelihood of temperatures exceeding the heat wave threshold are somewhat low, leading to non-significant trends in heat wave frequency, duration, and intensity (Table 4).

3.2 | Global model ensemble projections

Applying the bias correction technique outlined in section 2 (Hawkins *et al.*, 2013) to downscale each model in a 26-member ensemble reveals large cool biases in raw GCM output for NYC daily maximum records. We use kernel density estimates of daily maximum temperature for each ensemble member to quantify the impact of the statistical downscaling technique on mean and standard deviation statistics. As shown in Figure 4, models without bias correction, in general, underestimate observations on average by 2.7°C. This may be in part due to NYC's close proximity to the ocean, which may be included in some of the GCM's grid cell area. The statistical downscaling technique modifies the distribution of each ensemble member to more closely match that of the station observations. In addition, inter-model spread in mean and standard deviation is reduced during the reference period.

Bias-corrected mean daily maximum temperature (Figure 5a) shows a nearly linear trend in the high emissions scenario (RCP8.5), whereas rate of change in the stabilization scenario (RCP4.5) slows after 2040. RCP4.5 shows a linear trend of 0.3°C/decade, while RCP8.5 grows at a rate about three times faster, 0.69°C/decade. Model spread, quantified as 95% confidence intervals, become slightly wider towards the latter half of the century, covering a range of <1°C, while the band is closer to 0.5°C in the first half. At least a fraction of these observed long-term increases may be due upstream urbanization in New Jersey throughout the 20th century, as transitioned from agrarian land use to urban and suburban (Wichansky *et al.*, 2008). Zhang *et al.* (2009) showed that upstream urbanization may intensify UHI magnitude. He showed that for the city of Baltimore, MD, upstream urbanization accounted for up to 25% of the
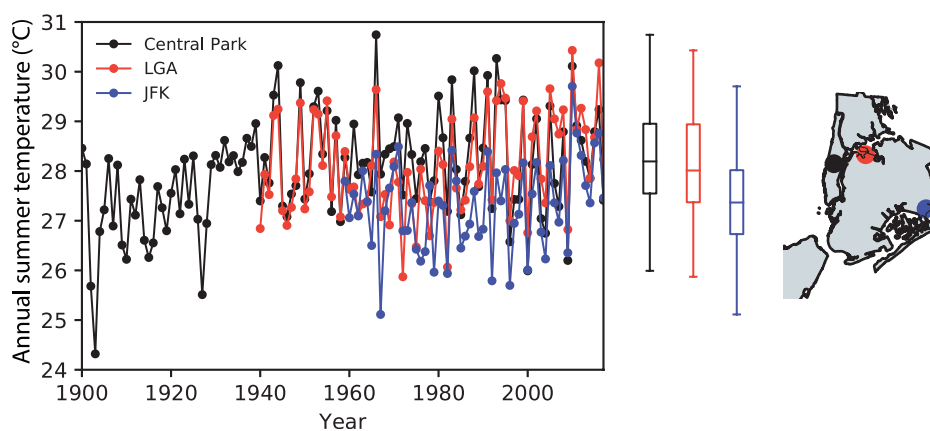
FIGURE 3 Annual daily maximum temperature trends from the Central Park (40.78 N, 73.97 W), LaGuardia (40.78 N, 73.89 W), and John F. Kennedy (40.64 N, 73.76 W) Airports. Box plots show distribution of annual mean maximum temperatures for the overlapping period recorded by all three stations (1959–2017). Boxes' lower and higher bounds represent each record's 25th and 75th percentiles, with centre lines showing its median. Lower and upper whiskers represent data lower and higher than 1.5 times the interquantile range. The map shows each station's geographical location [Colour figure can be viewed at wileyonlinelibrary.com]

T A B L E 4 Yearly trends of heat wave metrics in NYC

	Trend (1900–2017)	p value
Heat wave frequency (events per year)	.0059	.76
Mean heat wave duration (days per event)	.0036	.27
Mean heat wave intensity (°C)	−.0017	.56

Note: Trends are based on records from Central Park GHCN daily data from 1900 to 2017.

UHI magnitude. Meanwhile, uncorrected projections (Figure 5d) indicate similar increases in rate, albeit with a cooler ensemble mean. Differences between the two are larger in RCP8.5, where they grow from close to 3.25 to nearly 4.5°C by end of century, whereas in RCP4.5, their difference only changes by less than 0.5°C (Figure 5g).

Bias-corrected mean intensity, defined as the mean of event maximum temperatures in a given year (Figure 5b), grows at a rate nearly 0.3°C (RCP8.5) per decade, while the uncorrected record (Figure 5e) grows at 0.1°C/decade, nearly three times slower. RCP4.5 projections show a similar relationship between corrected and uncorrected records, although in general smaller, with 0.9 (corrected) to 0.3°C (uncorrected) per decade. Differences in ensemble mean (Figure 5h), however, grow larger over time between the two scenarios, with RCP8.5 and RCP4.5 being up to 2.5 and 1°C, respectively, over their uncorrected counterparts. Mean event duration projections (Figure 5c) are similar across

Daily maximum temperature KDE

FIGURE 4 Kernel density estimate (KDE) of 26 model, two-scenario ensemble before (blue) and after (red) histogram matching bias correction. Black curve represents airport observations KDE [Colour figure can be viewed at wileyonlinelibrary.com]

RCP4.5 and RCP8.5 up to the 2040s decade, similar to event intensity projections. Accelerating growth in projections of the latter half of the century are coupled with considerable increases in inter-model spread, with a 90% confidence band spanning ~10 days, compared to about 2 days in the first half. Average event duration in RCP8.5 grows from 5 days to over 25 days by end of century, with RCP4.5 growing from 5 to 7 days per event. This is due to both usage of a limited window for events to happen (i.e., June–July–August) as well as a constant temperature threshold for heat wave events. As mean daily temperatures surpass 32.22°C by the late 2050s, the likelihood of any given day surpassing this temperature increases. This might lead to separate events "coalescing" into longer lasting heat waves. It also explains why changes in this metric are much lower in uncorrected data (Figure 5), as temperatures are less likely to reach the heat wave threshold. These results compare favourably with the 35-model ensemble used in the 2015 New York City Panel for Climate Change analysis (Horton *et al.*, 2015), which only corrects for the mean of the temperature distribution (i.e., the *delta method*). However, when correcting for the standard deviation as well, end of century heat waves in RCP8.5 are both longer, and hotter.

The bias correction technique to downscale temperatures from GCM to local scale reduces differences between observation records by reducing biases in both the mean and variance of the model. Applying the technique to each model in the 26-member ensemble results in a reduction, in general, of inter-model spread, as all models are downscaled to the same historical record. This reduction does not hold for event duration, perhaps due to the uncertainty of event timing in addition to daily maximum temperatures involved in this metric. Another limitation of this approach is the assumption that the relationship between observations and GCM output will remain stationary for the entire projection period (Dixon *et al.*, 2016), which might not account for feedback processes such as additional anthropogenic heat and soil desiccation or moistening.

To partially address some of these limitations, we conducted a set of simulations using a state-of-the-art high-resolution urbanized regional climate model. This model depends on formulations of physical processes including many of the urban surface–atmosphere feedbacks that may modify heat wave conditions, rather than statistical relationships developed a priori or assumptions about the stationarity of bias correction parameters. These assumptions are particularly relevant for projections in NYC as it has been shown that the stationarity assumption may be violated in coastlines and especially in warm projections (Lanzante *et al.*, 2018), where grid cells may contain water, which in turn modifies near-surface temperatures.
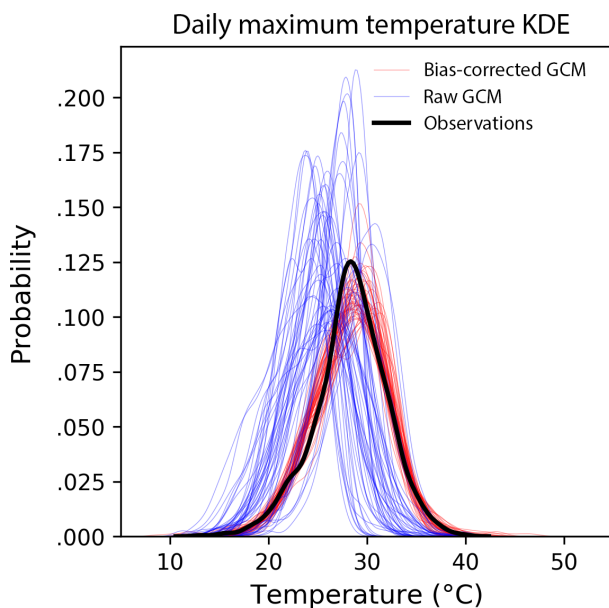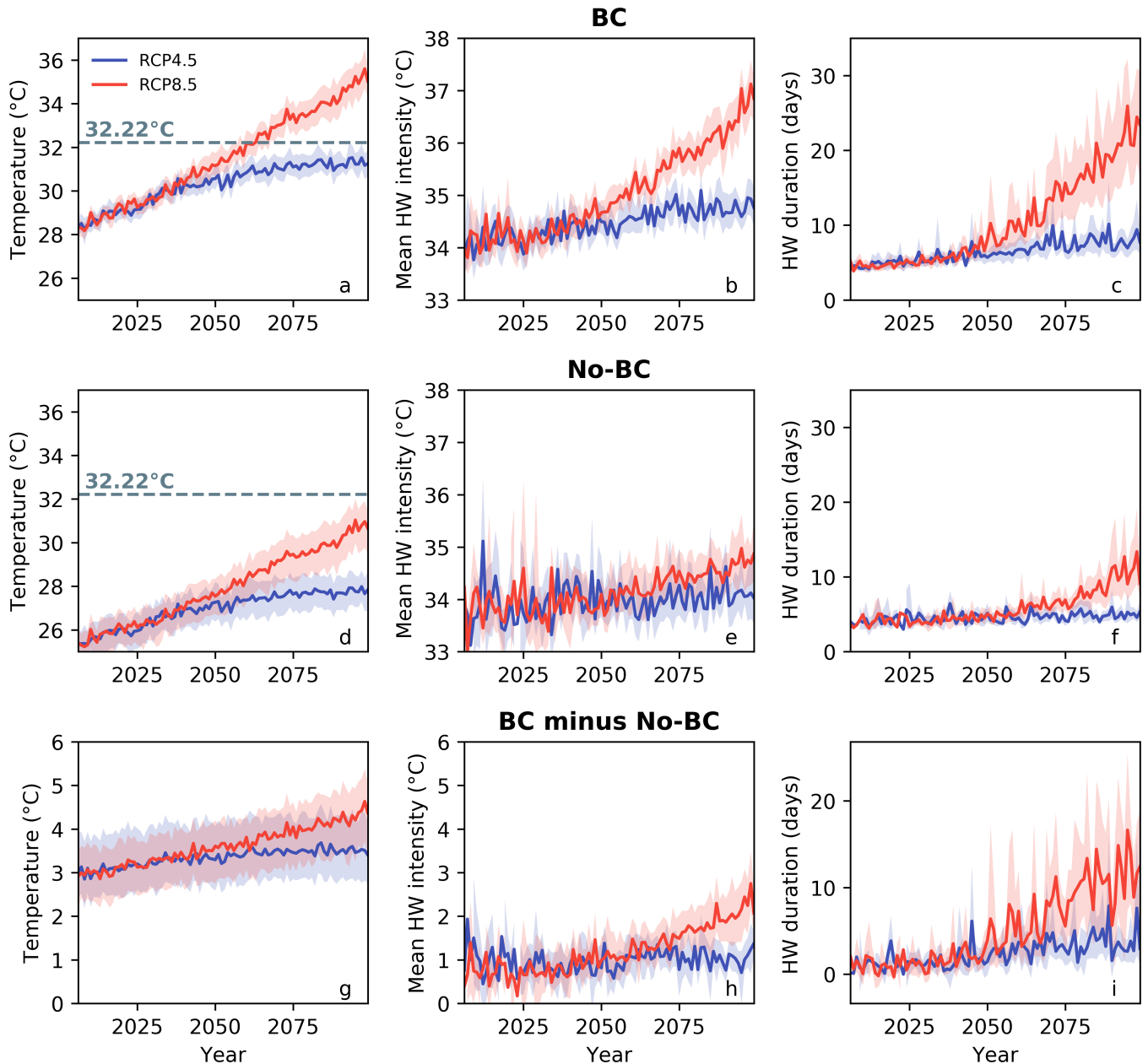
FIGURE 5 Daily maximum temperature and heat wave metric projections for NYC. Top row shows bias-corrected projections of daily maximum temperature (a), mean heat wave intensity (b), and mean heat wave duration (c). Centre row (d–f) shows the same metrics from uncorrected data, with the bottom row (g, i) showing the difference of the two. Solid blue and red bands indicate the 26-model ensemble mean, with shaded bands representing bootstrapped 95% confidence intervals. Grey dashed lines (a, d) show the temperature threshold for heat waves [Colour figure can be viewed at wileyonlinelibrary.com]

3.3 | High-resolution urbanized simulations

High-resolution regional climate models have been used to improve representation of precipitation and temperature (Antic *et al.*, 2004; Miller *et al.*, 2008; El-Samra *et al.*, 2017; Hughes *et al.*, 2017; Garuma *et al.*, 2018), especially in locations where complex surface processes are significant (e.g., mountains, coasts, and cities), although some studies have found geographically inconsistent accuracy improvements (Wang and Kotamarthi, 2015). In addition, high-resolution dynamical downscaling

methods have been used to derive projections of extreme events, such as heat waves (Gao *et al.*, 2012). Here, we employ advances in the representation of urban physics in the WRF model to project heat wave metrics throughout NYC. Our simulation approach focuses on three time periods representing contemporary (2006–2010), mid-century (2045–2049), and end of century (2095–2099) across the RCP4.5 and RCP8.5 scenarios.

Evaluating model output against weather station data (Central Park, LGA, and JFK) for the contemporary period

(2006–2010) reveals that WRF-simulated daily maximum temperature improves on the input bias-corrected Community Earth System Model (BC-CESM1) input data in both model mean and standard deviation (Figure 6a). Observations reported a mean daily maximum of 28.41°C with a standard deviation of 3.69°C. WRF simulations results, interpolated to weather station locations using nearest neighbour, showed a mean daily maximum of 28.66°C (0.25°C error) with a 3.37°C standard deviation (0.32 error), whereas BC-CESM1 showed a 26.54°C mean (1.87°C error) and 2.87°C standard deviation (0.82°C% error). These results are consistent with other studies (Bruyère et al., 2014), which found reduced cold biases in near-surface temperature distributions when forcing WRF with bias-corrected climate data.

On the other hand, mean daily minimum temperatures (Figure 6b) are overestimated by both BC-CESM1 and WRF simulations by 1.38 and 2.54°C, respectively. WRF simulations, however, improve on standard deviation, with an error of 0.04°C, while in BC-CESM1 the error reaches 0.31°C. Both WRF and BC-CESM1 reproduce the Weibull distribution of the 10-m winds. However, WRF underestimates calm wind conditions (<5 m/s), while slightly overestimating wind speeds >6 m/s compared to BC-CESM1. WRF does capture extreme wind conditions, with BC-CESM only reaching a maximum of 10 m/s, whereas WRF reaches up to 18 m/s, closer to the observed maximums of 22 m/s.

Limitations in BC-CESM1 are, in part, inherent to its coarse horizontal resolution (0.94 latitude × 1.24 longitude, ~100 km near NYC). Locations near the coast are especially vulnerable to these limitations, as a grid cell's area of influence includes both land and water, impacting its ability to reproduce observed temperature variance (Lanzante et al., 2018).

Mean heat wave intensity (Figure 7, left) projections show, in general, larger increases closer to the coast compared to inland locations. In the RCP4.5, heat wave intensity peaks in the mid-century period, with most of the city experiencing increases between 0 and 3°C. Increases are largest over the southeast part of the city, suggesting a weakening of the afternoon sea-breeze (Figure 8) that would typically keep this location cooler, as seen from the JFK station records (Figure 3). By end of century, meant event intensity ranges between 0.5 and 2°C, following a similar geographical pattern. In RCP8.5, event intensity increases throughout the century, with the largest anomalies observed in the latter half, similar to results in the statistically downscaled projections. Here, however, intensity anomalies range from 2 to 5°C.

As shown in Figure 8, simulations show an overall reduction in wind speeds. During the 10% coolest days, wind direction distribution is fairly similar, with southeast and southwesterly winds flow being the most common, albeit with an end of century reduction from 2.0–3.2 to 1.2–2.8 m/s. During the 10% warmest days, end-of-century wind directions exhibit a shift closer to southwesterly flows, potentially due, in part, to increased urban–rural temperature gradients. Warm days also show a similar wind speed reduction as in the 10% coolest days, marking an overall weakening of flow over the city, which may lead to increased UHI magnitudes as shown by previous studies (Li et al., 2016; Founda and Santamouris, 2017).

Mean event duration (Figure 7, right) anomalies display an almost opposite geospatial gradient compared to event intensity, with larger increases over Manhattan (west part of the city). In RCP4.5, events are projected to last 1–3 days longer than the contemporary period across both mid-
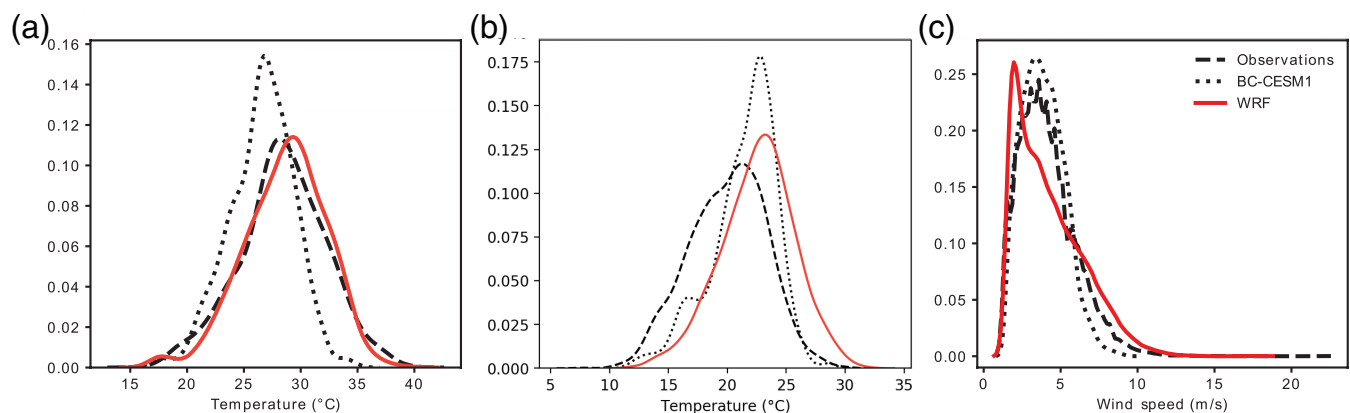
FIGURE 6 Distribution of modelled and observed (a) daily maximum temperatures, (b) daily minimum temperatures, and (c) daily average wind speed in NYC between 2006 and 2010. Distributions are represented by kernel density estimates of daily maximum temperature. Observations belong to the Central Park, JFK, and LGA Global Historical Climatology Network (GHCN) stations. BC-CESM1 refers to CESM1 bias mean-corrected data set used as initial and boundary conditions in the high-resolution simulations, where the closest land grid point to NYC was used. WRF refers to simulated dynamically downscaled data from grid points closest to the three weather stations [Colour figure can be viewed at wileyonlinelibrary.com]
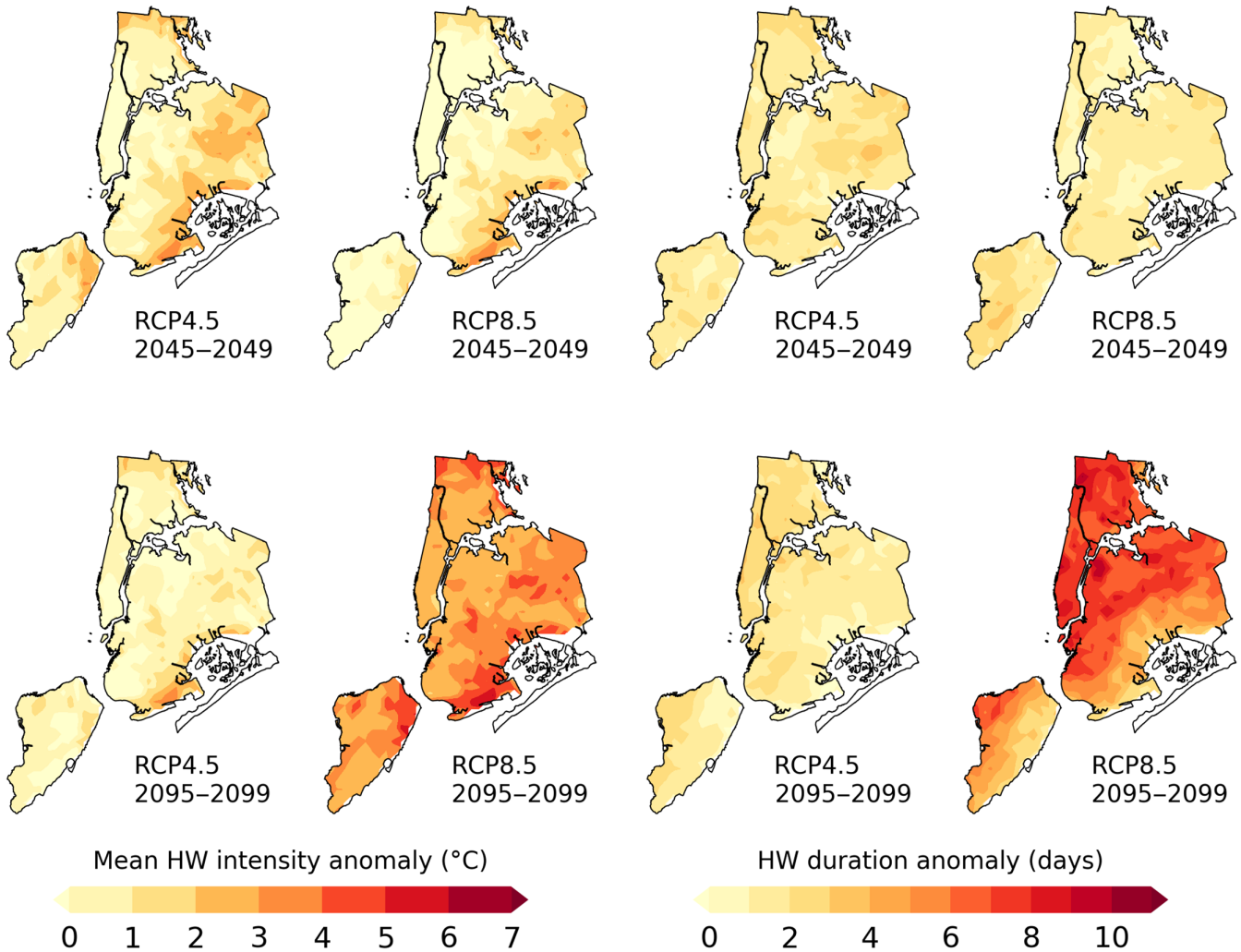
FIGURE 7 Dynamically downscaled median event intensity (left) and duration (right) for NYC. Anomalies are computed based on simulations of 2006–2010 summers (JJA) [Colour figure can be viewed at wileyonlinelibrary.com]

century and end of century, albeit with shifts in the location of the maxima. In RCP8.5, the mean event duration follows a similar geospatial pattern between mid-century and end of century as that of RCP8.5, reaching more than seven additional events. However, as in the single point projections, "coalescing events" are more likely to occur in RCP8.5. Excess heat wave days in densely packed parts of the city suggest that as summers become warmer, heat stored in buildings may play a role in extending event duration. In particular, lack of evapotranspiration due to impervious surfaces as well as heat storage in built structures may extend heat wave conditions heterogeneously throughout the city, coupled with increased anthropogenic heat from air conditioning. This heterogeneity is particularly important due to geographical differences in socioeconomic status of residents, translating to a difference in risk of heat impacts to health.

Studies have shown that water vapour content of air, in addition to ambient temperature, regulates the ability of humans to cool down via evaporation of sweat (Malchaire *et al.*, 2000). Simulated projections of water vapour mixing ratio changes (Figure 9a) appear to be sensitive to distance to the coast, as sea-breeze circulations bring moist ocean air to the city. Moreover, air conditioning systems contribute a portion of anthropogenic heat through evaporative cooling, further increasing atmospheric water vapour. Modelled changes increase with distance to the southern Long Island coastline, since warm air is able to hold more water, and this leads to increases in atmospheric water vapour. In the medium emissions scenario (RCP4.5), water vapour increases range between 0 and 14% across simulations 2045–2049, increasing to 6–18% by 2095–2099. In RCP8.5, mid-century changes are less than 4%, but balloon to 24–30% by end of century. The water vapour increases at the end of the century are larger closer to the coast potentially due to increased evaporation over the ocean.

Relative humidity, which measures the saturation of the atmosphere to water vapour, is projected to increase in all

FIGURE 8 Wind rose plots for selected grid points in Brooklyn, NY. Bar length represents normalized wind direction frequency, while colour map indicates wind speed magnitude [Colour figure can be viewed at wileyonlinelibrary.com]
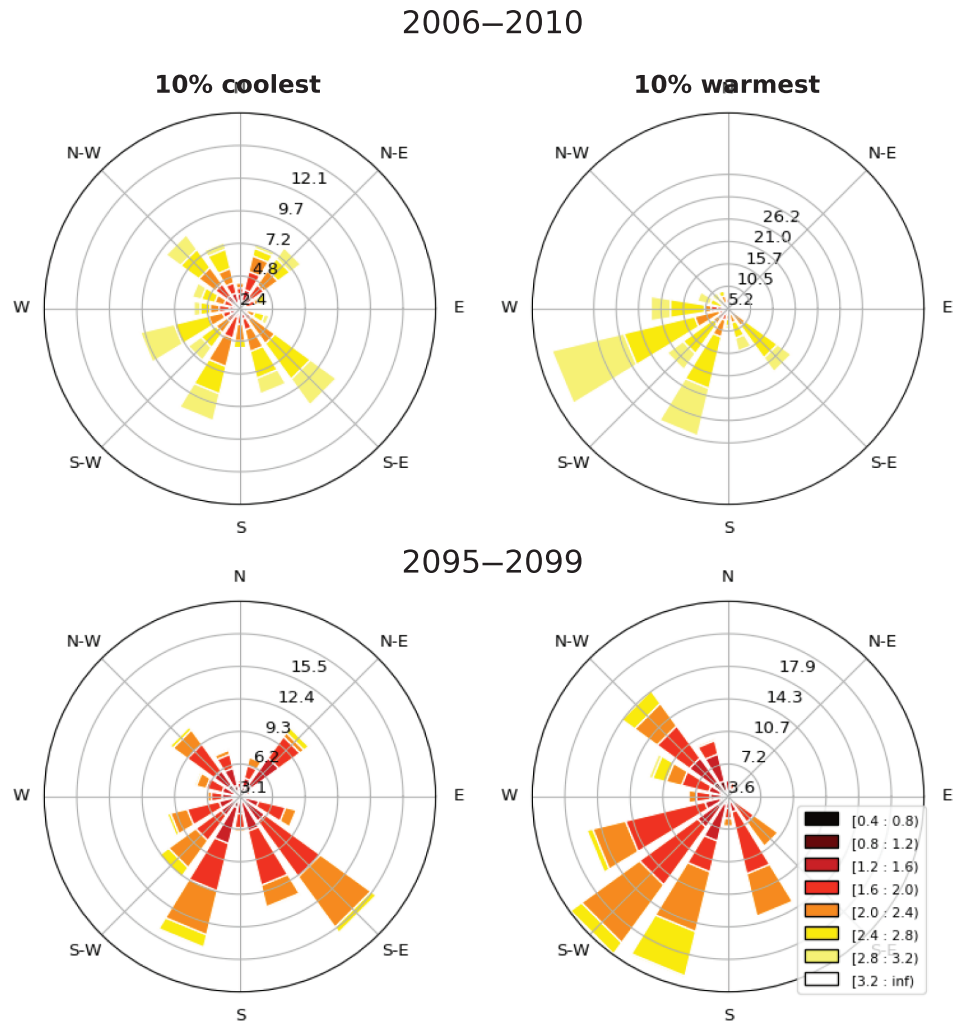
simulation periods and scenarios, except in end of century RCP8.5 (Figure 9b). This decrease indicates that capacity of air to carry water vapour, a function of temperature, is increasing at a faster pace than vapour is being added.

4 | CONCLUSIONS

Use of dynamical downscaling techniques accounts for statistical methods' shortcomings by improving resolution, and thus representation of heterogeneous urban surfaces, as well as inclusion of urban-specific processes. However, these new methods are computationally intensive, limiting the feasibility of multi-model, full-year ensembles, which are useful to better quantify projection uncertainties. Additionally, there are uncertainties in the temporal change of urban parameters such as land cover, building height, or building technology (e.g., higher air conditioning efficiency and improved thermal performance), which might modify urban–atmosphere interactions.

Lack of detailed information on parameters such as air conditioning adoption throughout the city and even building

occupancy schedules may also impact anthropogenic heat fluxes, necessitating partnerships with stakeholders at the building and city levels. As cities become more aware of upcoming challenges, however, they have started to enact laws to collect this information. One such example in NYC is "Local Law 84 of 2009," which mandates reporting of energy end use by buildings above certain loads. Research tools have also started to address these issues, as in the work of Xu *et al.* (2018), which introduces a "cooled fraction" parameter to BEM simulations.

Another limitation of this study is the assumption of a static urban canopy; no urban densification or impacts of population shifts are included. These limitations may be addressed with the use of city land cover and building projections, in turn highlighting the need for engagement with policymakers. Krayenhoff *et al.* (2018) offers a recent example of this approach, finding a geographically varying nonlinear relationship between urban expansion and global climate change signals throughout the United States. Techniques such as cellular automata models of urban land cover sprawl (Clarke *et al.*, 1997; Li and Yeh, 2002; Mitsova *et al.*, 2011) may be incorporated into high-resolution
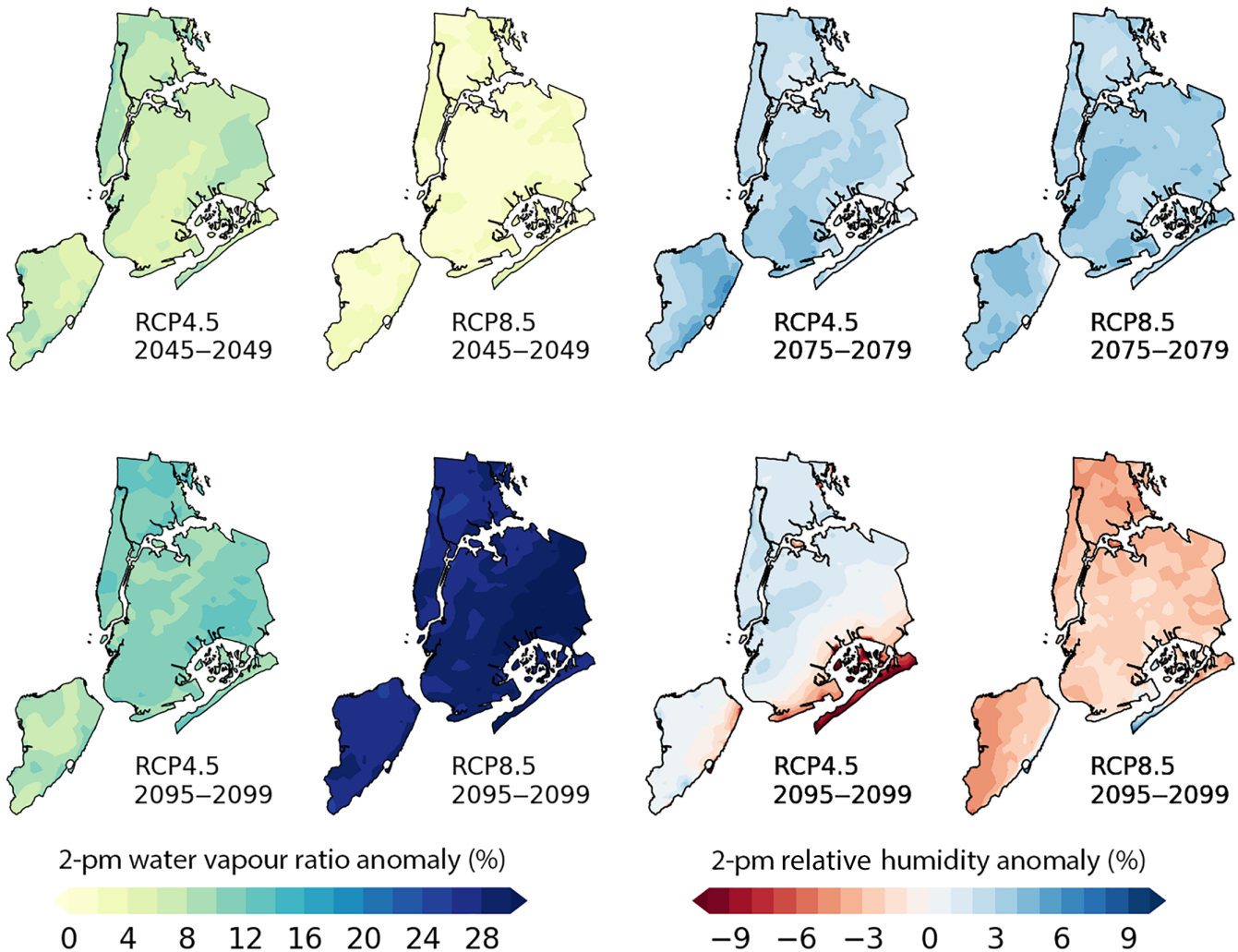
FIGURE 9 (a) Median 2-pm water vapour mixing ratio and (b) relative humidity anomaly over NYC at 2-m height [Colour figure can be viewed at wileyonlinelibrary.com]

simulations, as well as projections of building technology change to account for increases in cooling technology efficiency. Urban expansion and densification has been shown to contribute to local warming, in some instances, as much as warming associated with global climate change, as studies in Paris (Lemonsu *et al.*, 2015), Japan (Adachi *et al.*, 2012), Arizona (Georgescu *et al.*, 2012), and Sydney (Argüeso *et al.*, 2014) have shown, as does upwind urbanization (Zhang *et al.*, 2009).

Atmospheric water vapour projections showed overall increase across all scenarios and RCPs. However, future temperature increases in the dynamically downscaled CESM1 RCP8.5 scenario lead to higher capacity of air to hold water vapour, leading a decrease in relative humidity. This decrease may have considerable health impacts, as skin evaporative cooling via perspiration may not be as inhibited as in RCP4.5 and mid-century RCP8.5. These results do not imply, however, less risk of heat-related mortality, as

RCP8.5 still has large temperature increases compared to other scenarios.

The approach presented here provides useful insights on the interplay between regional and local climate and the potential for localized intensification of extreme heat. These insights may be useful for city-level stakeholders for planning of adaptation strategies for health and energy and may serve as a template for projections of extreme heat metrics for other cities.

ORCID

Luis E. Ortiz https://orcid.org/0000-0002-4248-6374

REFERENCES

Adachi, S.A., Kimura, F., Kusaka, H., Inoue, T. and Ueda, H. (2012) Comparison of the impact of global climate changes and

urbanization on summertime future climate in the Tokyo Metropolitan Area. *Journal of Applied Meteorology and Climatology*, 51(8), 1441–1454. https://doi.org/10.1175/JAMC-D-11-0137.1.

Anderson, G.B. and Bell, M.L. (2010) Heat waves in the United States: mortality risk during heat waves and effect modification by heat wave characteristics in 43 U.S. communities. *Environmental Health Perspectives*, 119(2), 210–218. https://doi.org/10.1289/ehp.1002313.

Anderson, G.B. and Bell, M.L. (2012) Lights out: impact of the August 2003 power outage on mortality in New York, NY. *Epidemiology*, 23(2), 189–193. https://doi.org/10.1097/EDE.0b013e318245c61c.

Antic, S., Laprise, R., Denis, B. and de Elía, R. (2004) Testing the downscaling ability of a one-way nested regional climate model in regions of complex topography. *Climate Dynamics*, 23(5), 473–493. https://doi.org/10.1007/s00382-004-0438-5.

Argüeso, D., Evans, J.P., Fita, L. and Bormann, K.J. (2014) Temperature response to future urbanization and climate change. *Climate Dynamics*, 42(7–8), 2183–2199. https://doi.org/10.1007/s00382-013-1789-6.

Bruyère, C.L., Done, J.M., Holland, G.J. and Fredrick, S. (2014) Bias corrections of global models for regional climate simulations of high-impact weather. *Climate Dynamics*, 43(7–8), 1847–1856. https://doi.org/10.1007/s00382-013-2011-6.

Clarke, K.C., Hoppen, S. and Gaydos, L. (1997) A self-modifying cellular automaton model of historical urbanization in the San Francisco Bay area. *Environment and Planning B: Planning & Design*, 24(2), 247–261. https://doi.org/10.1068/b240247.

Dixon, K.W., Lanzante, J.R., Nath, M.J., Hayhoe, K., Stoner, A., Radhakrishnan, A., Balaji, V. and Gaitán, C.F. (2016) Evaluating the stationarity assumption in statistically downscaled climate projections: Is past performance an indicator of future results? *Climate Change*, 135(3–4), 395–408. https://doi.org/10.1007/s10584-016-1598-0.

El-Samra, R., Bou-Zeid, E. and El-Fadel, M. (2017) To what extent does high-resolution dynamical downscaling improve the representation of climatic extremes over an orographically complex terrain? *Theoretical and Applied Climatology*, 134, 265–282. https://doi.org/10.1007/s00704-017-2273-8.

Founda, D. and Santamouris, M. (2017) Synergies between urban heat island and heat waves in Athens (Greece), during an extremely hot summer (2012). *Scientific Reports*, 7(1), 10973. https://doi.org/10.1038/s41598-017-11407-6.

Gaffin, S.R., Rosenzweig, C., Khanbilvardi, R., Parshall, L., Mahani, S., Glickman, H., Goldberg, R., Blake, R., Slosberg, R.B. and Hillel, D. (2008) Variations in New York City's urban heat island strength over time and space. *Theoretical and Applied Climatology*, 94(1–2), 1–11. https://doi.org/10.1007/s00704-007-0368-3.

Gao, Y., Fu, J.S., Drake, J.B., Liu, Y. and Lamarque, J.-F. (2012) Projected changes of extreme weather events in the eastern United States based on a high-resolution climate modeling system. *Environmental Research Letters*, 7(4), 044025. https://doi.org/10.1088/1748-9326/7/4/044025.

Garuma, G.F., Blanchet, J.-P., Girard, É. and Leduc, M. (2018) Urban surface effects on current and future climate. *Urban Climate*, 24, 121–138. https://doi.org/10.1016/j.uclim.2018.02.003.

Gedzelman, S.D., Austin, S., Cermak, R., Stefano, N., Partridge, S., Quesenberry, S. and Robinson, D.A. (2003) Mesoscale aspects of the urban heat island around New York City. *Theoretical and Applied Climatology*, 75(1–2), 29–42. https://doi.org/10.1007/s00704-002-0724-2.

Georgescu, M., Moustaoui, M., Mahalov, A. and Dudhia, J. (2012) Summer-time climate impacts of projected megapolitan expansion in Arizona. *Nature Climate Change*, 3(1), 37–41. https://doi.org/10.1038/nclimate1656.

Gutiérrez, E., González, J.E., Martilli, A. and Bornstein, R. (2015a) On the anthropogenic heat fluxes using an air conditioning evaporative cooling parameterization for mesoscale urban canopy models. *Journal of Solar Energy Engineering*, 137(5), 051005. https://doi.org/10.1115/1.4030854.

Gutiérrez, E., Martilli, A., Santiago, J.L. and González, J.E. (2015b) A mechanical drag coefficient formulation and urban canopy parameter assimilation technique for complex urban environments. *Boundary-Layer Meteorology*, 157(2), 333–341. https://doi.org/10.1007/s10546-015-0051-7.

Hawkins, E., Osborne, T.M., Ho, C.K. and Challinor, A.J. (2013) Calibration and bias correction of climate projections for crop modelling: an idealised case study over Europe. *Agricultural and Forest Meteorlogy*, 170, 19–31. https://doi.org/10.1016/j.agrformet.2012.04.007.

Hong, S.-Y. and Lim, J.-O.J. (2006) The WRF single-moment 6-class microphysics scheme (WSM6). *Asia-Pacific Journal of Atmospheric Sciences*, 42(2), 129–151.

Horton, R., Bader, D., Kushnir, Y., Little, C., Blake, R. and Rosenzweig, C. (2015) New York City panel on climate change 2015 report chapter 1: climate observations and projections. *Annals of the New York Academy of Sciences*, 1336(1), 18–35. https://doi.org/10.1111/nyas.12586.

Hughes, M., Lundquist, J.D. and Henn, B. (2017) Dynamical downscaling improves upon gridded precipitation products in the Sierra Nevada, California. *Climate Dynamics*. https://doi.org/10.1007/s00382-017-3631-z.

Kain, J.S. (2004) The Kain-Fritsch convective parameterization: an update. *Journal of Applied Meteorology*, 43(1), 170–181. https://doi.org/10.1175/1520-0450(2004)043<0170:TKCPAU>2.0.CO;2.

Krayenhoff, E.S., Moustaoui, M., Broadbent, A.M., Gupta, V. and Georgescu, M. (2018) Diurnal interaction between urban expansion, climate change and adaptation in US cities. *Nature Climate Change*, 8(12), 1097–1103. https://doi.org/10.1038/s41558-018-0320-9.

Lanzante, J.R., Dixon, K.W., Nath, M.J., Whitlock, C.E. and Adams-Smith, D. (2018) Some pitfalls in statistical downscaling of future climate. *Bulletin of the American Meteorological Society*, 99(4), 791–803. https://doi.org/10.1175/BAMS-D-17-0046.1.

Le Comte, D.M. and Warren, H.E. (1981) Modeling the impact of summer temperatures on national electricity consumption. *Journal of Applied Meteorology*, 20(12), 1415–1419. https://doi.org/10.1175/1520-0450(1981)020<1415:MTIOST>2.0.CO;2.

Lemonsu, A., Viguié, V., Daniel, M. and Masson, V. (2015) Vulnerability to heat waves: impact of urban expansion scenarios on urban heat island and heat stress in Paris (France). *Urban Climate*, 14, 586–605. https://doi.org/10.1016/j.uclim.2015.10.007.

Li, D. and Bou-Zeid, E. (2013) Synergistic interactions between urban heat islands and heat waves: the impact in cities is larger than the sum of its parts. *Journal of Applied Meteorology and Climatology*, 52(9), 2051–2064. https://doi.org/10.1175/JAMC-D-13-02.1.

Li, D., Sun, T., Liu, M., Wang, L. and Gao, Z. (2016) Changes in wind speed under heat waves enhance urban heat islands in the Beijing

Metropolitan Area. *Journal of Applied Meteorology and Climatology*, 55(11), 2369–2375. https://doi.org/10.1175/JAMC-D-16-0102.1.

Li, T., Horton, R.M. and Kinney, P.L. (2013) Projections of seasonal patterns in temperature-related deaths for Manhattan, New York. *Nature Climate Change*, 3(8), 717–721. https://doi.org/10.1038/nclimate1902.

Li, X. and Yeh, A.G.-O. (2002) Neural-network-based cellular automata for simulating multiple land use changes using GIS. *International Journal of Geographical Information Science*, 16(4), 323–343. https://doi.org/10.1080/13658810210137004.

Malchaire, J., Kampmann, B., Havenith, G., Mehnert, P. and Gebhardt, H.J. (2000) Criteria for estimating acceptable exposure times in hot working environments: a review. *International Archives of Occupational and Environmental Health*, 73(4), 215–220. https://doi.org/10.1007/s004200050420.

Martilli, A., Clappier, A. and Rotach, M.W. (2002) An urban surface exchange parameterisation for mesoscale models. *Boundary-Layer Meteorology*, 104(2), 261–304.

Meehl, G.A. and Tebaldi, C. (2004) More intense, more frequent, and longer lasting heat waves in the 21st century. *Science*, 305(5686), 994–997. https://doi.org/10.1126/science.1098704.

Menne, M.J., Durre, I., Vose, R.S., Gleason, B.E. and Houston, T.G. (2012) An overview of the global historical climatology network-daily database. *Journal of Atmospheric and Oceanic Technology*, 29(7), 897–910. https://doi.org/10.1175/JTECH-D-11-00103.1.

Miller, N.L., Hayhoe, K., Jin, J. and Auffhammer, M. (2008) Climate, extreme heat, and electricity demand in California. *Journal of Applied Meteorology and Climatology*, 47(6), 1834–1844. https://doi.org/10.1175/2007JAMC1480.1.

Mitsova, D., Shuster, W. and Wang, X. (2011) A cellular automata model of land cover change to integrate urban growth with open space conservation. *Landscape and Urban Planning*, 99(2), 141–153. https://doi.org/10.1016/j.landurbplan.2010.10.001.

Monaghan, A.J., Steinhoff, D.F., Bruyere, C.L. and Yates, D. (2014) *NCAR CESM global bias-corrected CMIP5 output to support WRF/MPAS research*. Boulder, CO: Research Data Archive, UCAR/NCAR. https://doi.org/10.5065/D6DJ5CN4.

Nakanishi, M. and Niino, H. (2006) An improved Mellor-Yamada Level-3 model: its numerical stability and application to a regional prediction of advection fog. *Boundary-Layer Meteorology*, 119(2), 397–407. https://doi.org/10.1007/s10546-005-9030-8.

National Weather Service. (2015) *NWS weather fatality, injury and damage statistics*. Silver Spring, MD: National Weather Service.

National Weather Service. (2018) *NWS New York, NY excessive heat page*. Silver Spring, MD: National Weather Service.

Oke, T.R. (1988) The urban energy balance. *Progress in Physical Geography*, 12(4), 471–508. https://doi.org/10.1177/030913338801200401.

Ortiz, L., González, J.E. and Lin, W. (2018a) Climate change impacts on peak building cooling energy demand in a coastal megacity. *Environmental Research Letters*, 13(9), 094008. https://doi.org/10.1088/1748-9326/aad8d0.

Ortiz, L.E., Gonzalez, J.E., Wu, W., Schoonen, M., Tongue, J. and Bornstein, R. (2018b) New York City impacts on a regional heat wave. *Journal of Applied Meteorology and Climatology*, 57(4), 837–851. https://doi.org/10.1175/JAMC-D-17-0125.1.

Piani, C., Weedon, G.P., Best, M., Gomes, S.M., Viterbo, P., Hagemann, S. and Haerter, J.O. (2010) Statistical bias correction of global simulated daily precipitation and temperature for the application of hydrological models. *Journal of Hydrology*, 395 (3–4), 199–215. https://doi.org/10.1016/j.jhydrol.2010.10.024.

Ramamurthy, P., González, J., Ortiz, L., Arend, M. and Moshary, F. (2017) Impact of heatwave on a megacity: an observational analysis of New York City during July 2016. *Environmental Research Letters*, 12(5), 054011. https://doi.org/10.1088/1748-9326/aa6e59.

Riahi, K., Rao, S., Krey, V., Cho, C., Chirkov, V., Fischer, G., Kindermann, G., Nakicenovic, N. and Rafaj, P. (2011) RCP 8.5—a scenario of comparatively high greenhouse gas emissions. *Climate Change*, 109(1–2), 33–57. https://doi.org/10.1007/s10584-011-0149-y.

Rosenthal, D.H., Gruenspecht, H.K. and Moran, E.A. (1995) Effects of global warming on energy use for space heating and cooling in the United States. *Energy Journal*, 16(2), 77–96.

Salamanca, F., Krpo, A., Martilli, A. and Clappier, A. (2010) A new building energy model coupled with an urban canopy parameterization for urban climate simulations—part I. Formulation, verification, and sensitivity analysis of the model. *Theoretical and Applied Climatology*, 99(3–4), 331–344. https://doi.org/10.1007/s00704-009-0142-9.

Santamouris, M., Papanikolaou, N., Livada, I., Koronakis, I., Georgakis, C., Argiriou, A. and Assimakopoulos, D. (2001) On the impact of urban climate on the energy consumption of buildings. *Solar Energy*, 70(3), 201–216. https://doi.org/10.1016/S0038-092X(00)00095-5.

Santiago, J.L., Coceal, O., Martilli, A. and Belcher, S.E. (2008) Variation of the sectional drag coefficient of a group of buildings with packing density. *Boundary-Layer Meteorology*, 128(3), 445–457. https://doi.org/10.1007/s10546-008-9294-x.

Schatz, J. and Kucharik, C.J. (2015) Urban climate effects on extreme temperatures in Madison, Wisconsin, USA. *Environmental Research Letters*, 10(9), 094024. https://doi.org/10.1088/1748-9326/10/9/094024.

Scott, A.A., Waugh, D.W. and Zaitchik, B.F. (2018) Reduced urban heat island intensity under warmer conditions. *Environmental Research Letters*, 13(6), 064003. https://doi.org/10.1088/1748-9326/aabd6c.

Skamarock, W., Klemp, J., Dudhia, J., Gill, D., Barker, D., Wang, W., Huang, X. and Duda, M. (2008) *A description of the Advanced Research WRF version 3*. Boulder, CO: NCAR Technical note NCAR/TN-475+STR. https://doi.org/10.5065/D68S4MVH.

Smith, T.T., Zaitchik, B.F. and Gohlke, J.M. (2013) Heat waves in the United States: definitions, patterns and trends. *Climate Change*, 118(3–4), 811–825. https://doi.org/10.1007/s10584-012-0659-2.

Taylor, K.E., Stouffer, R.J. and Meehl, G.A. (2012) An overview of CMIP5 and the experiment design. *Bulletin of the American Meteorological Society*, 93(4), 485–498. https://doi.org/10.1175/BAMS-D-11-00094.1.

Tewari, M., Chen, F., Wang, W., Dudhia, J., LeMone, M., Mitchell, K., Ek, M., Gayno, G., Wegiel, J. and Cuenca, R. (2004) Implementation and verification of the unified NOAH land surface model in the WRF model. In: *20th Conference on Weather Analysis and Forecasting/16th Conference on Numerical Weather Prediction, Seattle, WA*. Boston, MA: American Meteorological Society.

Thomson, A.M., Calvin, K.V., Smith, S.J., Kyle, G.P., Volke, A., Patel, P., Delgado-Arias, S., Bond-Lamberty, B., Wise, M.A., Clarke, L.E. and Edmonds, J.A. (2011) RCP4.5: a pathway for stabilization of radiative forcing by 2100. *Climate Change*, 109(1–2), 77–94. https://doi.org/10.1007/s10584-011-0151-4.

van Vuuren, D.P., Edmonds, J., Kainuma, M., Riahi, K., Thomson, A., Hibbard, K., Hurtt, G.C., Kram, T., Krey, V., Lamarque, J.-F., Masui, T., Meinshausen, M., Nakicenovic, N., Smith, S.J. and Rose, S.K. (2011) The representative concentration pathways: an overview. *Climate Change*, 109(1–2), 5–31. https://doi.org/10.1007/s10584-011-0148-z.

Wang, J. and Kotamarthi, V.R. (2015) High-resolution dynamically downscaled projections of precipitation in the mid and late 21st century over North America. *Earth's Future*, 3(7), 268–288. https://doi.org/10.1002/2015EF000304.

Wichansky, P.S., Steyaert, L.T., Walko, R.L. and Weaver, C.P. (2008) Evaluating the effects of historical land cover change on summertime weather and climate in New Jersey: land cover and surface energy budget changes. *Journal of Geophysical Research*, 113 (D10), D10107. https://doi.org/10.1029/2007JD008514.

Xu, X., Chen, F., Shen, S., Miao, S., Barlage, M., Guo, W. and Mahalov, A. (2018) Using WRF-urban to assess summertime air conditioning electric loads and their impacts on urban weather in Beijing. *Journal of Geophysical Research: Atmospheres*, 123, 2475–2490. https://doi.org/10.1002/2017JD028168.

Zhang, D.-L., Shou, Y.-X. and Dickerson, R.R. (2009) Upstream urbanization exacerbates urban heat island effects. *Geophysical Research Letters*, 36(24), L24401. https://doi.org/10.1029/2009GL041082.